Simulation design and optimization of amorphous silicon/crystalline silicon heterojunction solar cells based on localized p-n junctions

J. S. Wang, J. R. Yuan*, S. Q. Liu, X. H. Deng
Department of Physics, Nanchang University, Nanchang 330031, China

Hydrogenated amorphous silicon/crystalline silicon heterojunction solar cells are currently a hot research topic in the field of photovoltaics, where parasitic absorption due to hydrogenated amorphous silicon layers has not been effectively addressed. For this reason, amorphous silicon/crystalline silicon heterojunction solar cells with localized p-n junctions (HACL cells) have been designed, which can significantly improve the parasitic absorption losses while maintaining the original advantages such as high open-circuit voltage. In this paper, we mainly use ATLAS 2D simulation software to conduct device simulation and parameter optimization of HACL cells, and simulate the effects of factors such as passivation inlet region width, insulation layer width, emitter width, passivation inlet region doping concentration and substrate doping concentration on the cell performance, respectively.

(Received January 11, 2023; Accepted April 3, 2023)

Keywords: ATLAS simulation, Local junction, Conversion efficiency, Solar cell

1. Introduction

In the past decades, heterojunction solar cells based on hydrogenated amorphous silicon/crystalline silicon (a-Si:H/c-Si) have attracted much attention due to their high open-circuit voltage, low-cost manufacturing process and low temperature coefficient [1-9]. In 1992, Sanyo (later acquired by Panasonic) developed an a-Si:H/c-Si heterojunction solar cell with intrinsically thin layers (referred to as HIT solar cell). For HIT solar cells, the doped a-Si:H layer located at the cell surface acts as the emitter, and the intrinsic a-Si:H layer acts as a passivation defect. However, the a-Si:H material has a high light absorption coefficient, which results in large light absorption losses. Holman et al [10] theoretically demonstrated that the relative efficiency of heterojunction solar cells can be improved by more than 5% by reducing parasitic absorption. To reduce the absorption loss of a-Si:H, several research teams have proposed to improve the parasitic absorption by using the interdigitated back contact (IBC) technique in silicon-based heterojunction solar cells [11-15] . Solar cells combining HIT and IBC technologies have achieved a world record conversion efficiency of over 26% [12,13] . However, the cell structures using HIT and IBC technologies are very complex and do not facilitate mass production. Our team proposed a new amorphous silicon/crystalline silicon heterojunction solar cell with localized p-n junction (a-Si:H/c-Si heterojunction with localized p-n structure, or HACL cell) [16-18] . The localized p-n

* Corresponding author: yuanjiren@ncu.edu.cn
https://doi.org/10.15251/DJNB.2023.182.423

junction can significantly improve the parasitic absorption loss of a-Si:H and reduce the recombination of photogenerated carriers in the emitter, and also maintain the high open-circuit voltage of the cell, while this cell structure is simplified compared to the HIT+IBC structure, which is convenient for mass production.

In this paper, the HACL cell structure was constructed mainly using the ATLAS device simulator[19,20], and the effects of passivation region width, insulating layer width, emitter width, doping concentration in passivation and inlet regions, and substrate doping concentration on the performance of HACL cells were investigated.

2. Physical models and simulation parameters

Figure 1(a) shows the device structure used in this simulation. The device structure is a crystalline silicon heterojunction bifacial solar cell structure with a local amorphous silicon emitter [16] , with an n-type crystalline silicon wafer as the substrate. The emitter side is divided into the emitter-conducting region and the passivation-inlet region. The emitter-conducting region is consists of an intrinsic amorphous silicon passivation layer (a-Si:H(i)), a heavily doped p-type amorphous silicon layer (a-Si:H(p)), and a metal grid line. The passivation-inlet region is consists of a heavily doped n-type crystalline silicon field passivation layer and a SiNx passivation and reflection reduction layer. The back-electric field side is divided into a back-electric field-conducting region and a passivation-inlet region. The back-electric field-conducting region is consists of an intrinsic amorphous silicon passivation layer (a-Si:H(i)), a heavily doped n-type amorphous silicon layer (a-Si:H(n)), and a metal grid line, and the passivation-inlet region is consists of a heavily doped n-type crystalline silicon field passivation layer, a SiNx passivation and reflection reduction layer. It is worth noting that an insulating layer is inserted between the passivation-inlet area and the conductive area to insulate the passivation-inlet area and the conductive area, and SiNx is used for this simulation. The initial values of the widths of the regions set in the simulation are 1000 μm for the passivation region, 500 μm for the insulation layer, and 100 μm for the emitter. The passivation-inlet area and conductive area are cross-distributed without overlapping, and Figure 1(b) illustrates a top view of the periodic structure of the device.

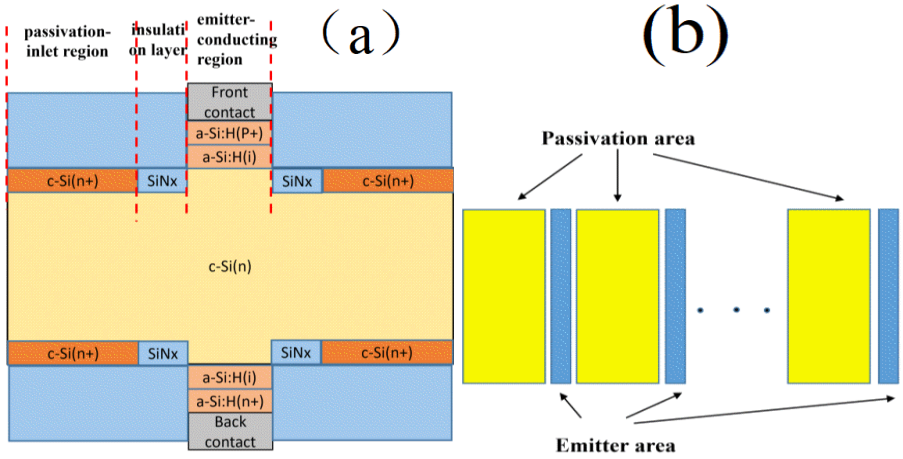

Fig. 1. (a) HACL cell structure diagram; (b) Top view of HACL cell.

The ATLAS device simulation module of Silvaco TCAD software is used in this study, and the simulation method is based on Poisson's equation and the electron and hole continuity equations.

$$div(\varepsilon\nabla\psi) = -\rho \tag{1}$$

where ψ is the electrostatic potential, ε is the local permittivity, and ρ is the local space charge density. Here ρ is the sum of the effects of all moving and fixed charges (including electrons, holes, and ionized impurities).

$$\frac{\partial n}{\partial t} = \frac{1}{q} div\, J_{n^+} G_n - R_n \tag{2}$$

$$\frac{\partial p}{\partial t} = -\frac{1}{q} div\, J_{p^+} G_p - R_p \tag{3}$$

where n and p are electron and hole concentrations, J_n and J_p are electron and hole current densities, G_n and G_p are electron and hole generation rates, R_n and R_p are electron and hole recombination rates, and q is the magnitude of the electron charge.

For a-Si:H materials, the density of states in the band gap has been confirmed to have both acceptor-like states (located in the upper half of the band gap) and donor-like states (located in the lower half of the band gap). Both the acceptor-like and donor-like states consist of an exponential band tail state (caused by bond angle distortion) and a Gaussian band gap state (caused by dangling bonds). The conduction and valence band tail states can be described as follows.

$$g_{A(E)} = G_{AO}\, exp\left(\frac{E-E_C}{E_A}\right) \tag{4}$$

$$g_{D(E)} = G_{DO}\, exp\left(\frac{E_V-E}{E_D}\right) \tag{5}$$

where G_{AO} and G_{DO} are the densities of states on E_V and E_C, respectively, E_A is an characteristic energy that determines the slope of the band tail extension into the band gap, and E_D is another characteristic energy that indicates how fast the band tail extends into the band gap.

The Gaussian mid-gap states of the acceptor-like and donor-like states are given by the following equations:

$$g_A(E) = N_{AG}\left\{-\frac{1}{2}\left[\frac{(E-E_{Ak})^2}{\sigma_A^2}\right]\right\} \tag{6}$$

$$g_D(E) = N_{DG}\left\{-\frac{1}{2}\left[\frac{(E-E_{Dk})^2}{\sigma_D^2}\right]\right\} \tag{7}$$

where N_{AG} and N_{DG} denote the density of states of the Gaussian acceptor and donor, respectively, E_{Ak} and E_{Dk} are the Gaussian peak energy locations, and σ_A and σ_D are the standard deviations of the Gaussian acceptor and donor.

The initial values of the main material and structural parameters used in this simulation are shown in Table 1 [21-23] , and the numerical calculation methods used in the simulation are the Newton iterative method and the Gummel iterative method. The recombination models used are Shockley-Read-Hall (SRH) recombination model, auger recombination model (Auger), and optical recombination model (optr); the mobility model related to the doping concentration, and the bandgap narrowing model due to heavy doping are also used. The simulated light conditions are AM 1.5G, 100 mW/cm^2, considering ground reflected light, with the temperature of 300 K.

Table 1. Main parameters used for the simulation.

Parameters and units	a-Si:H(p+)	a-Si:H(i)	a-Si:H(n+)	c-Si(n)	c-Si(n+/p+)
Thickness/nm	10	10	10	1.5×10^5	20
Electron affinity/eV	3.8	3..8	3.8	4.05	4.05
Band gap/eV	1.72	1.72	1.72	1.12	1.12
Relative dielectric constant	11.9	11.9	11.9	11.9	11.9
Effective conduction band density/cm^{-3}	2.5×10^{20}	2.5×10^{20}	2.5×10^{20}	2.8×10^{19}	2.8×10^{19}
Effective valence band density/cm^{-3}	2.5×10^{20}	2.5×10^{20}	2.5×10^{20}	1.04×10^{19}	1.04×10^{19}
Electron mobility/cm^2.v^{-1}.s^{-1}	10	20	10	1350	1350
Hole mobility/cm^2.v^{-1}.s^{-1}	2	5	2	450	450
Donor concentration/cm^{-3}	0	0	1×10^{19}	3×10^{15}	1×10^{18}
Acceptor concentration/cm^{-3}	6×10^{18}	0	0	0	1×10^{18}

3. Results and discussion

The cell defined by the parameters listed in Table 1 is the starting point of our simulation work. On this basis, ATLAS is used to simulate the effects of different parameter settings on the performance of the cell so as to investigate the carrier transport characteristics of the HACL cell and thus to further optimize its parameters.

3.1. Effect of passivation inlet region and insulating layer width on the performance of HACL cells

Keeping the other parameters constant, we simulated the effect of the width of the passivation inlet region on the cell performance with the insulating layer width as the second parameter. Figure 2 shows the simulation results that the short-circuit current density (Jsc), open-circuit voltage (Voc), fill factor (FF) and conversion efficiency of the HACL cell with the

width of the passivation region when the width of SiNx insulation layer is 100μm, 300μm, 500μm and 800μm, respectively. It can be seen that the width of the SiNx insulating layer has a small effect on the open-circuit voltage and the filling factor of the cell within the studied range, and the open-circuit voltage and the filling factor of the cell increase with the decrease of the width of the SiNx insulating layer at the same width of the passivation inlet region. The values of the open-circuit voltage and the filling factor of the cell tend to converge when the width of the passivation inlet region increases. From Fig. 2(a), we can see that the short-circuit current density of the cell is sensitive to the change of the width of the passivation zone when the insulating layer width is small (100 μm), and the maximum and minimum values of the short-circuit current density are obtained when the insulating layer width is 100 μm in the range of the width of the passivation range in this study, while the variation of short-circuit current density and conversion efficiency is relatively small when the insulating layer width is 300μm, 500μm and 800μm. When the width of the insulation layer is 100μm, the short-circuit current density of the cell increases with the width of the passivation inlet region, and when the width of the insulation layer is 300μm, 500μm and 800μm, the short-circuit current density of the cell increases with the width of the passivation inlet region and then decreases, and when the width of the insulation layer decreases, the width of the passivation inlet region corresponding to the maximum short-circuit current density of the cell increases. This is because the increase in the width of the passivation region of the cell can increase the light absorption area of the cell and produce more photogenerated carriers, but the increase in width will also lead to an increase in the transverse transport distance of more photogenerated carriers (including the transverse transport distance of photogenerated carriers in the passivation region and the transverse transport distance of the insulating layer) and an increase in the chance of carrier recombination. At the beginning, the gain of increased photogenerated carriers due to the increase in the width of the passivation inlet area is greater than the loss due to the increase in the carrier transverse transport recombination caused by the increase in width, the carrier collected at the electrode increases, the short-circuit current density increases, with the increase in the width of the passivation inlet area, the gain due to the increase in the optical absorption area and the loss due to the carrier transverse transport recombination tend to balance, the short-circuit current density reaches the maximum, with the further increase of the width of the passivation inlet area, the gain brought by the increase of the light absorption area is not enough to offset the loss brought by the carrier transverse transport complex, and the short-circuit current density starts to decrease [19] . Figure 3 shows the transport characteristics of the substrate carriers at the emitter side. It can be seen that the heavily doped passivated inlet region forms a high-low junction with the substrate, creating an electric field toward the substrate on the substrate surface, so that the photogenerated few carriers (in this case, holes) generated near the passivated inlet region can be driven to the interior of the substrate, and the photogenerated few carriers driven to the interior of the substrate are transported laterally near the emitter and finally collected by the emitter conducting region. From Fig. 2(d), the cell can achieve the best conversion efficiency when the insulating layer width is small. In this simulation, the maximum value of cell conversion efficiency is achieved at a passivation inlet region width of 1200 μm when the insulating layer width is 100 μm.

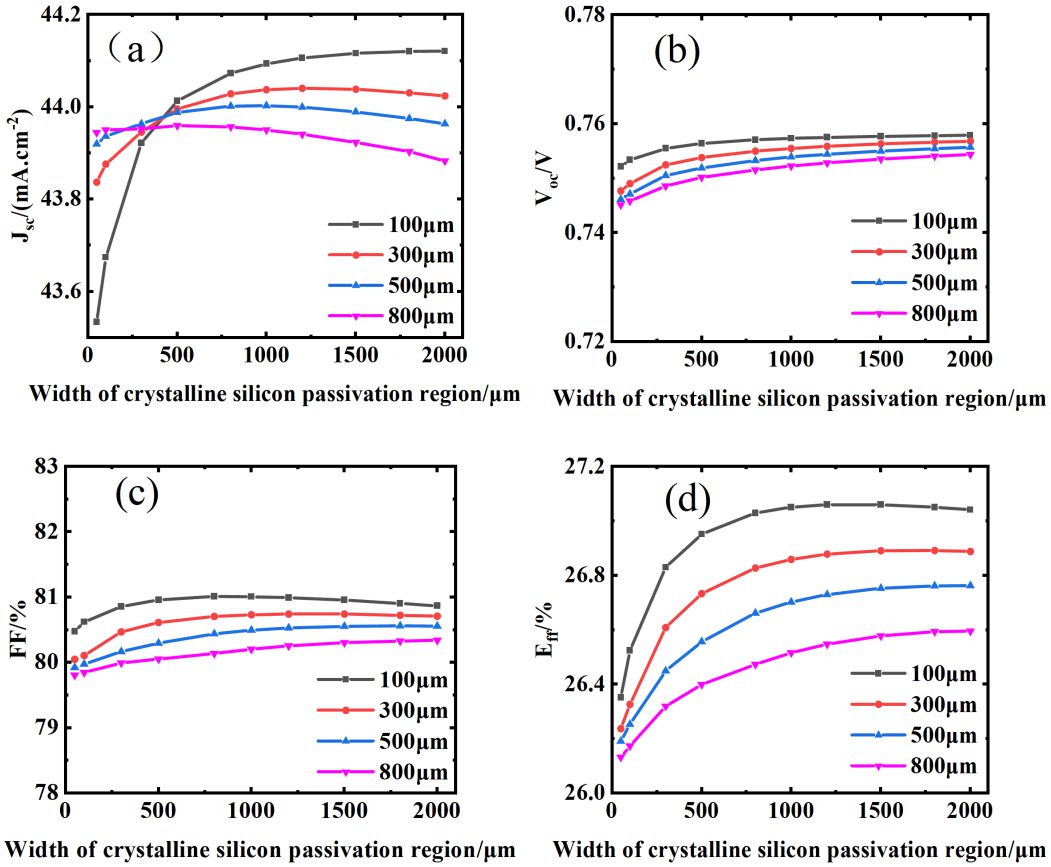

Fig. 2. Effect of passivation inlet region width on HACL cells.

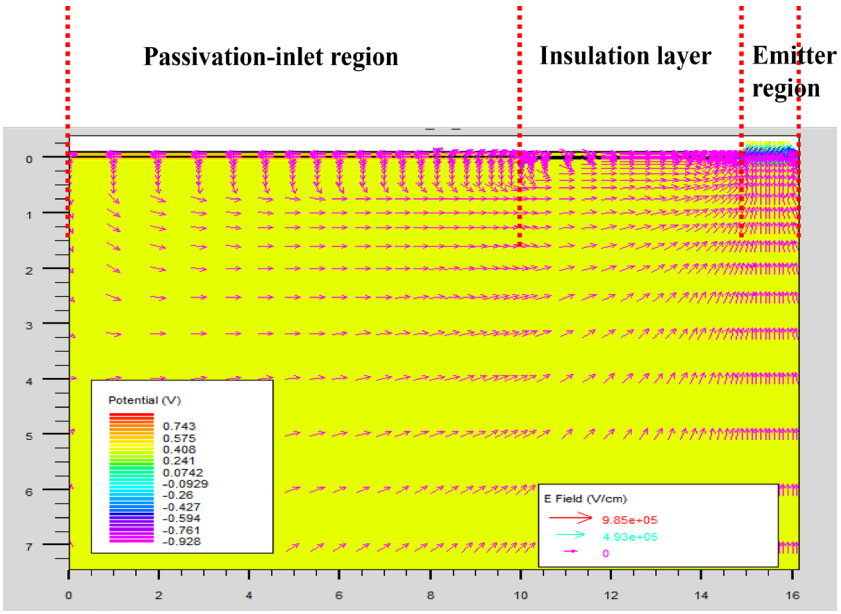

Fig. 3. Potential and electric field diagram near the emitter side of HACL cell.

3.2. Effect of emitter width on HACL cell performance

We adjusted the width of the insulating layer and the passivation inlet area to the optimized width (i.e., 100 μm for the insulating layer and 1200 μm for the passivation inlet area), and kept the other parameters unchanged to investigate the effect of the emitter width on the HACL cell. As shown in Fig. 4, the short-circuit current decreases with the increase of emitter width, the open-circuit voltage is basically not affected by the change of emitter width, the filling factor increases rapidly and then slowly with the increase of emitter width, and the conversion efficiency increases rapidly and then decreases slowly under the combined influence of the above factors, the highest conversion efficiency is achieved when the emitter width is 200μm (7.14% of the whole light-access area).

Because the a-Si:H layer of the emitter has a high light absorption coefficient, the number of photons absorbed in the substrate region covered by it becomes low, and thus fewer photogenerated carriers are generated. Figure 5 shows the generation rate of photogenerated carriers near the emitter side, where different colors represent different rates of photogenerated carrier generation. It can be seen from the figure that near the emitter side, the generation rate of photogenerated carriers in the substrate region covered by the emitter (X-axis 15 to 16 region in the figure) is lower than other regions, so the short-circuit current density of the cell decreases as the width of the emitter increases. The emitter width increases and the series resistance of the cell decreases, so the fill factor of the cell increases.

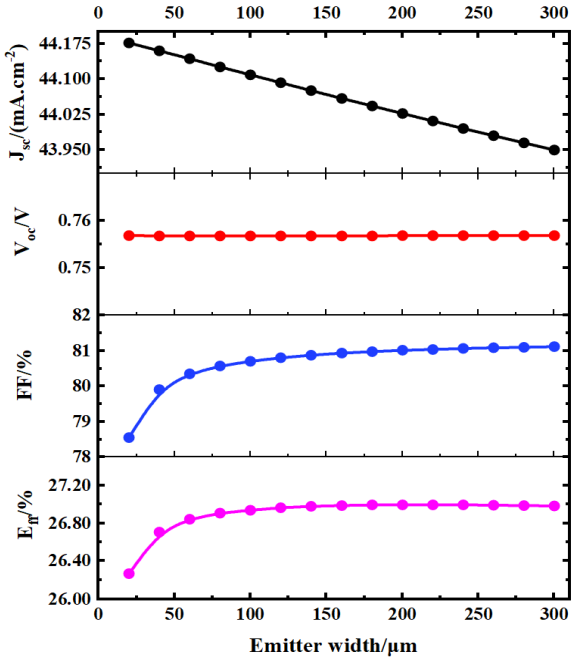

Fig. 4. Effect of emitter width on HACL cell.

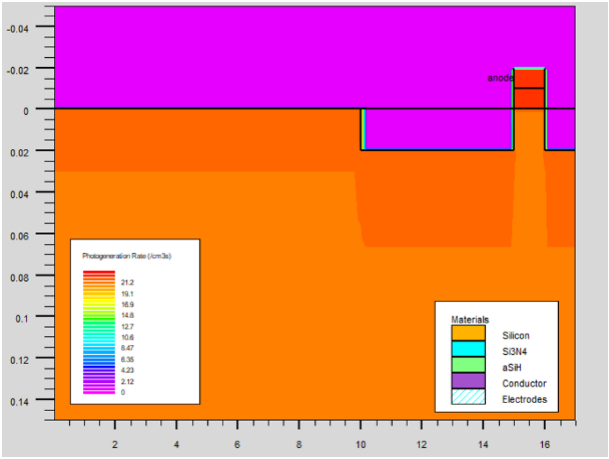

Fig. 5. Generation rates of photogenerated carriers in different regions near the emitter side.

3.3. Effect of doping concentration in the passivation inlet region on the performance of HACL cells

We adjusted the width of passivation inlet area, insulating layer width and emitter width to the optimal state, and changed the doping concentration of passivation inlet area at the emitter side while keeping the doping concentration of passivation inlet area at the back-electric field side as Table 1 value and changed the doping concentration of passivation inlet area at the back-electric field side while keeping the doping concentration of passivation inlet area at the emitter side as Table 1 value, respectively, to investigate the effect of doping concentration of passivation inlet area at the emitter side and the back-electric field side on HACL cells. Figure 5 shows the effect of varying the doping concentration from 5×10^{16} cm^{-3} to 1×10^{20} cm^{-3} in the passivated inlet region of the emitter side and the passivated inlet region of the back-electric field side on the performance of the HACL cell.

It can be seen that except for the difference in the magnitude of short-circuit current density decrease at high doping (1×10^{19} cm^{-3} to 1×10^{20} cm^{-3}), the trends of the other performance parameters of the HACL cell are almost the same with the doping concentration in the passivation inlet region of the emitter side and the passivation inlet region of the back-electric field side. The short-circuit current density of the cell increases slightly at the beginning with the increase of the doping concentration in the passivation inlet area, and then remains basically unchanged. When the doping concentration is relatively high (greater than 3×10^{18} cm^{-3}), the short-circuit current density of the cell starts to decrease, and the open-circuit voltage rises slowly at the beginning with the increase of the doping concentration. When the doping concentration exceeds 3×10^{18} cm^{-3}, the open-circuit voltage starts to decrease and the rate of decrease has a tendency to accelerate. The trend of filling factor is different from that of the open-circuit voltage, and the filling factor decreases slightly with the increase of the doping concentration when the doping concentration is low, but starts to increase rapidly when the doping concentration is high. Under the combined influence of the above factors, the conversion efficiency of the cell shows a slow increase at the beginning and then a rapid decrease, and the best conversion efficiency is achieved when the doping concentration in the passivation region is 3×10^{18} cm^{-3}.

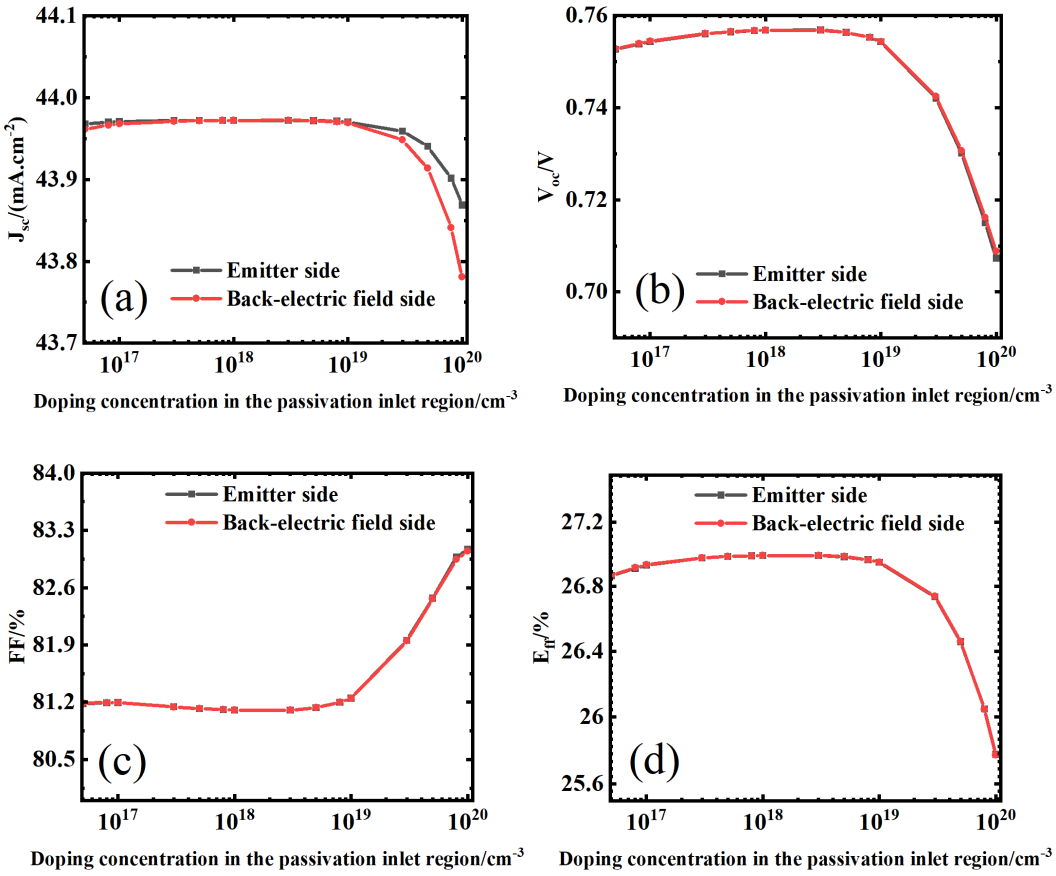

Fig. 6. Effect of doping concentration in the emitter side passivated inlet region and doping concentration in the back-electric field side passivated inlet region on the performance of HACL cells.

Fig. 7 shows the auger recombination rate and electric field intensity of the passivated inlet region at the emitter side under different doping concentrations of the passivated inlet region. It can be seen that as the doping concentration of the passivation inlet region increases, the auger recombination rate of the passivation inlet region increases rapidly, and the electric field strength at the high-low junction formed between the heavily doped passivation inlet region and the substrate also increases rapidly. The increased electric field strength at the high-low junction can better reflect the photogenerated carriers, thus reducing the surface recombination, which is conducive to improving the short-circuit current density of the cell. At the same time, the reduction of surface recombination will also reduce the reverse saturation current of the cell, which is beneficial to increase the open-circuit voltage of the cell. When the doping concentration in the passivation inlet area becomes quite high, the auger recombination in the passivation inlet area begins to have a relatively large impact on the performance of the cell. The greater the doping concentration in the passivation inlet area, the greater the auger recombination rate, so that when the passivation inlet area is highly doped, the short-circuit current density of the cell decreases, and the open-circuit voltage of the cell decreases due to the increased reverse saturation current at this time. Due to the special structure of HACL cell, the photogenerated carriers generated near the passivation inlet area need to travel a long lateral distance to be collected by the electrode, which

will lead to an increase in the series resistance of the transport and thus affect the filling factor. The passivation inlet region of HACL cell has low resistivity due to high doping concentration, which can be regarded as a low resistance channel for the lateral transport of photogenerated carriers, thus reducing the lateral transport distance of photogenerated carriers in the high resistance cell body region and decreasing the series resistance loss caused by the lateral transport of photogenerated carriers, and the filling factor of the cell will be improved.

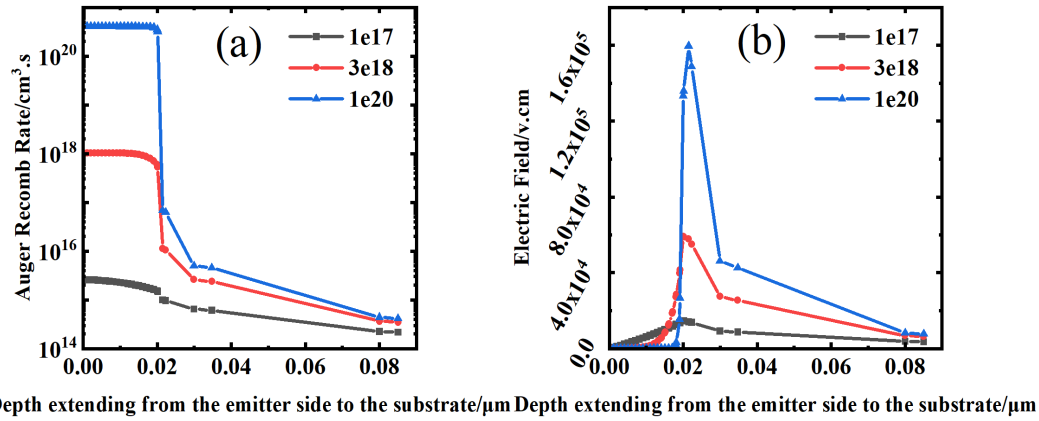

Fig. 7. The auger recombination and electric field intensity near the passivation inlet region of the emitter side at different doping concentrations of the passivation inlet region, where the X-axis range from 0 to 0.02 is the heavily doped passivation inlet region.

3.4 Effect of substrate doping concentration on the performance of HACL cells

Under the conditions that the width of the passivation inlet region, the width of the insulation layer, the width of the emitter, and the doping concentration of the passivation inlet region are adjusted to the optimal level, and other parameters are kept constant, Fig. 8 shows the effect of the change of the substrate doping concentration on the performance of the HACI cell, which varies from 3×10^{15} cm^{-3} to 1×10^{17} cm^{-3}. From the figure, we can see that the short-circuit current density of the cell decreases as the concentration of the substrate increases, and the rate of decrease becomes faster as the concentration increases, and when the doping concentration of the substrate reaches 1×10^{17} cm^{-3}, the short-circuit current density decreases to 42.9mA/cm^2. While the open-circuit voltage remains essentially constant at doping concentrations less than 5×10^{16} cm^{-3}, it decreases slightly when the doping concentration is greater than 5×10^{16} cm^{-3}, from the original 0.76 V to 0.75 V. At doping concentrations less than 6×10^{16} cm^{-3}, the fill factor increases with the doping concentration, from 81% at the beginning to 84.99%, while when the doping value decreases slightly when the doping concentration is greater than this value. The conversion efficiency, on the other hand, shows a numerical increase followed by a decrease under the combined effect of the above factors, and the cell reaches the maximum conversion efficiency at a substrate doping concentration of 4×10^{16} cm^{-3}.

The recombination and generation of substrate photogenerated carriers for substrate doping concentrations of 2×10^{16} cm^{-3} and 1×10^{17} cm^{-3} are given in Fig. 9. Where the X-axis value equals to 0 μm is the light-receiving surface of the substrate, the X-axis value equals to 150 μm is the backlight surface of the substrate, and the Y-axis value is treated by taking the logarithm. It can

be seen from Fig. 9(a) that with the increase of the substrate doping concentration, the recombination rate of photogenerated carriers increases in most regions of the substrate except for the part of the region near the light-receiving surface, while it can be seen from Fig. 9(b) that the generation rate of photogenerated carriers does not increase with the increase of the substrate doping concentration, and then the number of photogenerated carriers in the substrate becomes relatively lower. In addition, the relative diffusion length of carriers decreases as the substrate doping concentration increases, which further decreases the collection rate of photogenerated carriers by the electrode, so the short-circuit current density of the cell decreases as the substrate doping concentration increases. The carrier recombination rate of the substrate increases with the increase of the substrate doping concentration; the reverse saturation current of the cell increases and the open-circuit voltage of the cell decreases. The conductivity of the substrate increases with the increase of the substrate doping concentration, so when the substrate doping concentration increases, the series resistance of the cell decreases and the fill factor increases.

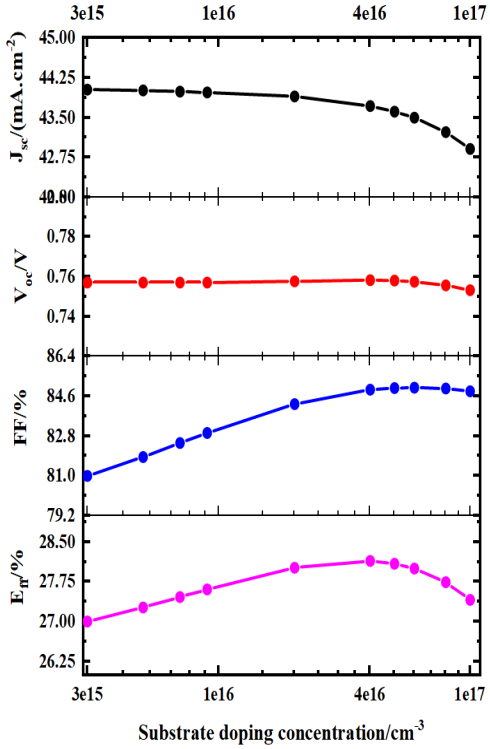

Fig. 8. Effect of substrate doping concentration on HACL cell.

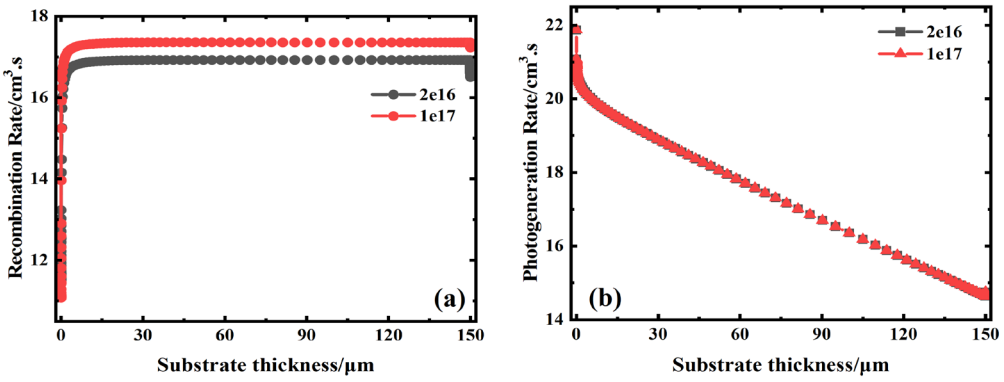

Fig. 9. Recombination rate, generation rate of photogenerated carriers in substrates with different substrate doping concentrations

3.5. Cell performance after parameter optimization

The parameters optimized by the preliminary simulation are: width of passivation inlet region (1200 μm), width of insulation layer (100 μm), width of emitter (200 μm), doping concentration of passivation inlet region at the emitter side and the back-electric field side (3×10^{18} cm^{-3}) and doping concentration of substrate (4×10^{16} cm^{-3}), the conversion efficiency of HACL cell obtained from the above optimized parameters can reach28.07%. The I-V curve of the optimized cell is shown in Fig. 10. From the optimized IV curve, it can be seen that the HACL cell has the characteristics of both high open-circuit voltage and large short-circuit current.

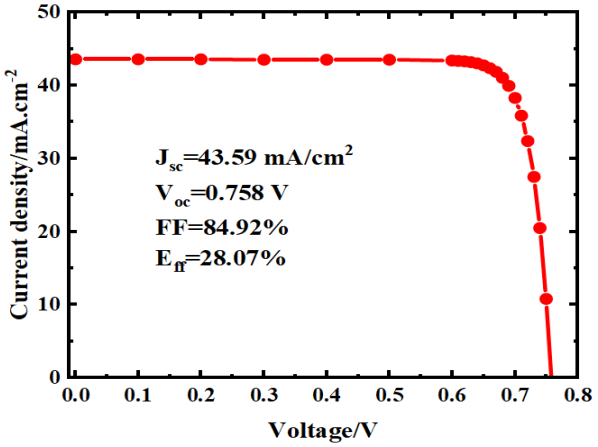

Fig. 10. IV curve of the optimized HACL cell.

4. Conclusion

A crystalline silicon heterojunction bifacial solar cell structure (HACL) with a localized amorphous silicon emitter was modeled using ATLAS software. The effects of passivation inlet region width, insulation layer width, emitter width, passivation inlet region doping concentration and substrate doping concentration on the HACL cell performance were simulated. The results show that the width of the passivation inlet region mainly affects the conversion efficiency by influencing the short-circuit current density, and a narrow insulating layer width is a prerequisite for optimizing the width of the passivation inlet region to achieve the best conversion efficiency. The conversion efficiency of the cell shows a pattern of increasing and then decreasing with the increase of the values of the passivation inlet region width, emitter width, passivation inlet region doping concentration and substrate doping concentration. The optimized area ratio of passivation inlet area, insulating layer and emitter area is 12:1:2. The optimized doping concentration of passivation inlet region is $3\times10^{18}cm^{-3}$, and the optimized doping concentration of substrate is $4\times10^{16}cm^{-3}$. The conversion efficiency of the HACL cells can reach 28.07%, which indicates that this kind of solar cell with localized p-n junction is a promising photovoltaic device.

Acknowledgements

This work was supported by the National Natural Science Foundation of China (No. 11964018) and the Jiangxi Provincial Natural Science Foundation (No. 20224BAB202032).

References

[1] W.M. Alkharasani, N. Amin, S.A. Shahahmadi, A.A. Alkahtani, I.S.B. Mohamad, P. Chelvanathan, T.S. Kiong, Materials 15(10), 3508(2022); https://doi.org/10.3390/ma15103508

[2] M.Q. Khokhar, S.Q. Hussain, D.P. Pham, S. Lee, H. Park, Y. Kim, E.-C. Cho, J. Yi, Energies 13(7), 1635(2020); https://doi.org/10.3390/en13071635

[3] Z. Wu, L. Zhang, R. Chen, W. Liu, Z. Li, F. Meng, Z. Liu, Applied Surface Science 475, 504(2019); https://doi.org/10.1016/j.apsusc.2018.12.239

[4] M.A. Green, Y. Hishikawa, E.D. Dunlop, D.H. Levi, J. Hohl-Ebinger, M. Yoshita, A.W.Y. Ho-Baillie, Progress in Photovoltaics: Research and Applications 27(1), 3(2019); https://doi.org/10.1002/pip.3102

[5] L. Zhao, G. Wang, H. Diao, W. Wang, Journal of Physics D: Applied Physics 51(4), 045501(2018); https://doi.org/10.1088/1361-6463/aa9ecd

[6] Y. Yao, X. Xu, X. Zhang, H. Zhou, X. Gu, S. Xiao, Materials Science in Semiconductor Processing 77, 16(2018); https://doi.org/10.1016/j.mssp.2018.01.009

[7] H. Bashiri, M.A. Karami, S. Mohammadnejad, Superlattices and Microstructures 120, 327(2018); https://doi.org/10.1016/j.spmi.2018.05.056

[8] M. Taguchi, A. Yano, S. Tohoda, K. Matsuyama, Y. Nakamura, T. Nishiwaki, K. Fujita, E. Maruyama, IEEE Journal of Photovoltaics 4(1), 96(2014); https://doi.org/10.1109/JPHOTOV.2013.2282737

[9] M. Tanaka, M. Taguchi, T. Matsuyama, T. Sawada, S. Tsuda, S. Nakano, H. Hanafusa, Y. Kuwano, Japanese Journal of Applied Physics 31(Part 1, No. 11), 3518(1992); https://doi.org/10.1143/JJAP.31.3518

[10] Z.C. Holman, A. Descoeudres, L. Barraud, F.Z. Fernandez, J.P. Seif, S.D. Wolf, C. Ballif, IEEE Journal of Photovoltaics 2(1), 7(2012); https://doi.org/10.1109/JPHOTOV.2011.2174967

[11] M. Lu, S. Bowden, U. Das, R. Birkmire, Applied Physics Letters 91(6), 063507(2007); https://doi.org/10.1063/1.2768635

[12] K. Yoshikawa, H. Kawasaki, W. Yoshida, T. Irie, K. Konishi, K. Nakano, T. Uto, D. Adachi, M. Kanematsu, H. Uzu, K. Yamamoto, Nature Energy 2(5), 17032(2017); https://doi.org/10.1038/nenergy.2017.32

[13] K. Yoshikawa, W. Yoshida, T. Irie, H. Kawasaki, K. Konishi, H. Ishibashi, T. Asatani, D. Adachi, M. Kanematsu, H. Uzu, K. Yamamoto, Solar Energy Materials and Solar Cells 173, 37(2017); https://doi.org/10.1016/j.solmat.2017.06.024

[14] M.A. Green, E.D. Dunlop, J. Hohl-Ebinger, M. Yoshita, N. Kopidakis, X. Hao, Progress in Photovoltaics: Research and Applications 29(7), 657(2021); https://doi.org/10.1002/pip.3444

[15] T. Sugiura, S. Matsumoto, N. Nakano, IEEE Transactions on Electron Devices 68(11), 5645(2021); https://doi.org/10.1109/TED.2021.3112136

[16] H. Huang, L. Zhou, J. Yuan, C.Gao, Z.Yue, Patent CN108336157A, (2018).

[17] J. Yuan, L. Zhou, H. Huang, C.Gao, Z.Yue, Patent CN108461569A, (2018).

[18] H. Huang, L. Zhou, J. Yuan, Z. Quan, Chinese Physics B 28, 128503(2019); https://doi.org/10.1088/1674-1056/ab5212

[19] A. M. Laoufi, B. Dennai, O. Kadi, M. Fillali, Chalcogenide Letters 18(6), 297(2021);

https://doi.org/10.15251/CL.2021.186.297

[20] M. Fillali, B. Dennai, Journal of Ovonic Research 15(5), 279(2019).

[21] Y. Ichikawa, R. Ishikawa, M. Konagai, AIP Advances 12(6), 065006(2022); https://doi.org/10.1063/5.0094626

[22] H. Huang, G. Tian, L. Zhou, J. Yuan, W.R. Fahrner, W. Zhang, X. Li, W. Chen, R. Liu, Chinese Physics B 27(3), 038502(2018); https://doi.org/10.1088/1674-1056/27/3/038502

[23] N. Hernández-Como, A. Morales-Acevedo, Solar Energy Materials and Solar Cells 94(1), 62(2010); https://doi.org/10.1016/j.solmat.2009.05.021